







Research Article

Supersonically Sprayed Flexible ZnO/PVDF Composite Films with Enhanced Piezoelectricity for Energy Harvesting and Storage

Devi Prashad Ojha ^{1,2}, Bhavana Joshi,³ Edmund Samuel,⁴ Ashwin Khadka ³,
Ali Aldalbahi ⁵, Govindasami Periyasami ⁵, Daekyu Choi,^{1,2} Seongpil An ^{1,2,6}
and Sam S. Yoon ³

¹SKKU Advanced Institute of Nanotechnology (SAINT), Sungkyunkwan University (SKKU), Suwon 16419, Republic of Korea

²Department of Nano Science and Technology, Sungkyunkwan University (SKKU), Suwon 16419, Republic of Korea

³School of Mechanical Engineering, Korea University, Seoul 02841, Republic of Korea

⁴Energy Environment Policy and Technology, Graduate School of Energy and Environment (KU-KIST Green School), Korea University, Seoul 02841, Republic of Korea

⁵Department of Chemistry, College of Science, King Saud University, Riyadh 11451, Saudi Arabia

⁶Department of Nano Engineering, Sungkyunkwan University (SKKU), Suwon 16419, Republic of Korea

Correspondence should be addressed to Seongpil An; esan@skku.edu and Sam S. Yoon; skymoon@korea.ac.kr

Received 4 April 2023; Revised 1 May 2023; Accepted 23 June 2023; Published 13 July 2023

Academic Editor: Tholkappiyan Ramachandran

Copyright © 2023 Devi Prashad Ojha et al. This is an open access article distributed under the Creative Commons Attribution License, which permits unrestricted use, distribution, and reproduction in any medium, provided the original work is properly cited.

A flexible piezoelectric nanogenerator (PENG) was developed to convert ambient mechanical energy into electrical energy. Highly crystalline template-free zinc oxide (ZnO) microrods were prepared using a wet chemical method at a low temperature. As-synthesized ZnO microrods were blended with polyvinylidene fluoride (PVDF) to prepare a piezoelectric composite film using the supersonic spraying method. A PENG electrode comprising ZnO microrods (0.5 g) produced 15.2 V under a tapping force of 20 N at 5 Hz. In addition, an output current of 32 μA was produced with a maximum power density of 12.5 $\mu\text{W cm}^{-2}$. The output voltage considering various body movements was investigated to demonstrate the flexibility and durability of the proposed PENG. Furthermore, the supercapacitive properties of ZnO/reduced graphene oxide were studied.

1. Introduction

The development of energy-harvesting technologies to meet the increasing energy demand has garnered considerable attention in the research community [1–3]. The harvesting of ambient energy, e.g., vibrational, wind, thermal, and solar energies, is being actively explored for advanced energy-harvesting applications based on the pyroelectric, piezoelectric, and triboelectric principles [4, 5]. In particular, mechanical energy harvesting using piezoelectric nanogenerators (PENGs) is a promising alternative source of clean energy owing to their stability in moist and dusty environments [6]. Piezoelectricity is defined as the potential difference that develops across the two surfaces of a piezoelectric film owing to the deformation of crystal struc-

tures under a mechanical force that causes electrical charge to flow through an electrical circuit.

Inorganic (e.g., lead zirconium titanate [7], lead titanate [8], barium titanate [9], zinc oxide [10], gallium nitride [11]) and organic piezoelectric materials (e.g., polyvinylidene fluoride (PVDF), polydimethylsiloxane, and Teflon [12]) have been used as PENG electrodes. With regard to output voltage/current performance, these materials can effectively power sensors, light-emitting diodes (LEDs), and biomedical and environmental monitoring devices using ambient mechanical forces [13]. In particular, zinc oxide (ZnO) is an effective PENG electrode material owing to its excellent piezoelectric characteristics, abundance, chemical stability, and nontoxicity [14–16]. ZnO exhibits the highest

piezoelectricity among semiconductors in groups II–IV [17] owing to its noncentrosymmetric hexagonal wurtzite structure, in which four O^{2-} ions surround a central Zn^{2+} ion in a tetragonal atomic arrangement. ZnO crystals temporarily deform under an applied force, causing the displacement of Zn and O atoms and consequently forming Zn^{2+} (cations) and O^{2-} (anions), which result in the development of piezoelectric potential [6, 18, 19].

Wang and Song [20] used piezoelectric ZnO nanowire (NW) arrays to convert mechanical energy into electrical energy. In their experiment, a strain field was generated owing to the bending of ZnO NWs, leading to the distribution of charge across the NWs. Based on the aforementioned study, multifunctional PENGs have been developed for intelligent wearable devices and sensors owing to their low weight, scalability, high flexibility, and simple fabrication process [21–24]. However, despite the high piezoelectric coefficient (d_{33}) of inorganic ceramic materials, their rigidity and fragility pose a challenge to wearable PENG devices.

To overcome the brittleness of piezoceramics, the addition of piezopolymers to piezoceramics has been investigated; this addition enhances the overall piezoelectric performance regarding durability and output voltage [25]. Semicrystalline PVDF is an important piezoelectric polymer used in flexible PENGs owing to its reasonable piezoelectric coefficient, excellent thermal and chemical resistance, biocompatibility, and high flexibility [25, 26]. Currently, five crystalline polymorphs of PVDF (α , β , γ , δ , and ϵ phases) have been identified [27]. Among them, the nonpolar α phase polymorph contributes to the mechanical strength of a PENG, whereas the β phase contributes to piezoelectricity. Consequently, the β phase amount must be increased to maximize power output. Several techniques, e.g., stretching, poling under a high electric field, electrospinning, and impregnation with inorganic and organic materials, have been employed to increase the polar and piezoactive β phase content in PVDF [25, 26]. The incorporation of inorganic materials with different morphologies into PVDF enhances its piezoelectric behavior owing to an increase in the β phase content and subsequent interfacial polarization [28–31]. Similarly, adding PVDF to rod-like ZnO results in a composite with enhanced piezoelectric behavior, and wearable electronic devices based on the resultant ZnO/PVDF (ZP) composite exhibit enhanced flexibility and longevity. Moreover, the piezoelectric properties of ZP composites depend on the ZnO content, preparation, and interactions between the two materials [32, 33].

In this study, ZnO microrods with PVDF were supersonically sprayed to fabricate piezocomposite films. Supersonic spray deposition is scalable, nonvacuum, and fast and, thus, considered a commercially viable method for industrial production [34–38]. In addition, the α phase of PVDF can be transformed into the polar β phase based on the shear stress inflicted by supersonic impact between ZnO and PVDF, thereby increasing the piezoelectricity and output power of the films [39]. This study determines the optimal combination of ZnO and PVDF that produces excellent piezoelectric properties. In addition, the excellent mechanical stability and durability of PENGs are demonstrated by introducing tapping, bending, and other body mechanical loads.

2. Experimental Methods

2.1. Materials. Zinc nitrate hexahydrate ($(Zn(NO_3)_2 \cdot 6H_2O)$, 98%, Sigma-Aldrich, USA), hexamethylenetetramine (HMTA, 99%, Sigma-Aldrich, USA), and sodium hydroxide (NaOH, 98%, Sigma-Aldrich, USA) were used as reagents to synthesize ZnO microrods. Furthermore, N,N-dimethylformamide (DMF, 99.8%, Sigma-Aldrich, USA), PVDF ($M_w \sim 534,000$, Sigma-Aldrich, USA), and synthesized ZnO microrods were used to fabricate the flexible ZP composite films. Reduced graphene oxide (rGO, N002-PDR, Angstrom Materials, USA), polyacrylonitrile (PAN, molecular weight 150 kDa, Sigma-Aldrich), and DMF were used for the fabrication of the ZnO/rGO electrode. The aqueous electrolyte 6 M KOH (Biosesang, South Korea) was used for electrochemical measurements.

2.2. Synthesis of ZnO Microrods. We prepared ZnO microrods using a simple wet chemical method, wherein 50 mL of 50 mM aqueous $Zn(NO_3)_2 \cdot 6H_2O$ solution and 50 mL of equimolar HMTA solution were blended in a 200 mL beaker. To maintain the pH of the solution at 7, a 4 M aqueous NaOH solution was used. The solution was vigorously stirred for 30 min at 25°C to complete the nucleation of ZnO. Finally, the turbid white solution was stirred in a closed container at 80°C for 5 h (Figure 1(a)). The resulting white precipitate was washed several times with a 1:1 water-ethanol mixture and dried overnight in an oven at 80°C.

2.3. Preparation of the ZnO/PVDF Composite Film. The ZnO/PVDF (ZP) precursor solution was prepared by mixing various proportions of ZnO microrods and PVDF powder in 30 mL of DMF. The weight of ZnO and PVDF in precursor solutions are listed in Table 1. Each suspension was vigorously stirred at 70°C for 10 h to homogeneously distribute the ZnO microrods in the PVDF/DMF mixture and prevent agglomeration. The ZP composite films are hereafter denoted as ZP4, ZP5, and ZP6 based on the masses of the ZnO microrods (0.4, 0.5, and 0.6 g, respectively (Table 1)).

The obtained solutions were used to fabricate ZP composite films via supersonic spraying [40, 41]. A typical supersonic spraying setup comprises an air compressor, air heater, and convergent-divergent supersonic nozzle (de Laval nozzle). An atomizer connected to a syringe pump was used to atomize the prepared solutions. In other words, the atomized solution of the composite material was accelerated by a supersonic air stream and deposited on a copper foil. The preheating temperature and pressure of the carrier gas (i.e., air in this study) during supersonic spraying were 250°C and 0.4 MPa, respectively. The supersonically blown composite material was deposited on a Cu foil attached to a X-Y moving stage (Figure 1(b)). The supersonic spraying technique has been explained in other studies [42, 43].

2.4. Fabrication of ZnO/PVDF-Based PENGs. The PENGs developed herein were fabricated using a 3 cm × 3 cm ZP composite film, 5 cm × 5 cm Cu foil, and 5 cm × 5 cm bare Cu tape. Two 0.5 cm × 5 cm Cu foil stripes acted as the positive and negative terminals (Figure 1(c)). Finally, the Cu foil | ZP composite film | Cu tape was encapsulated and

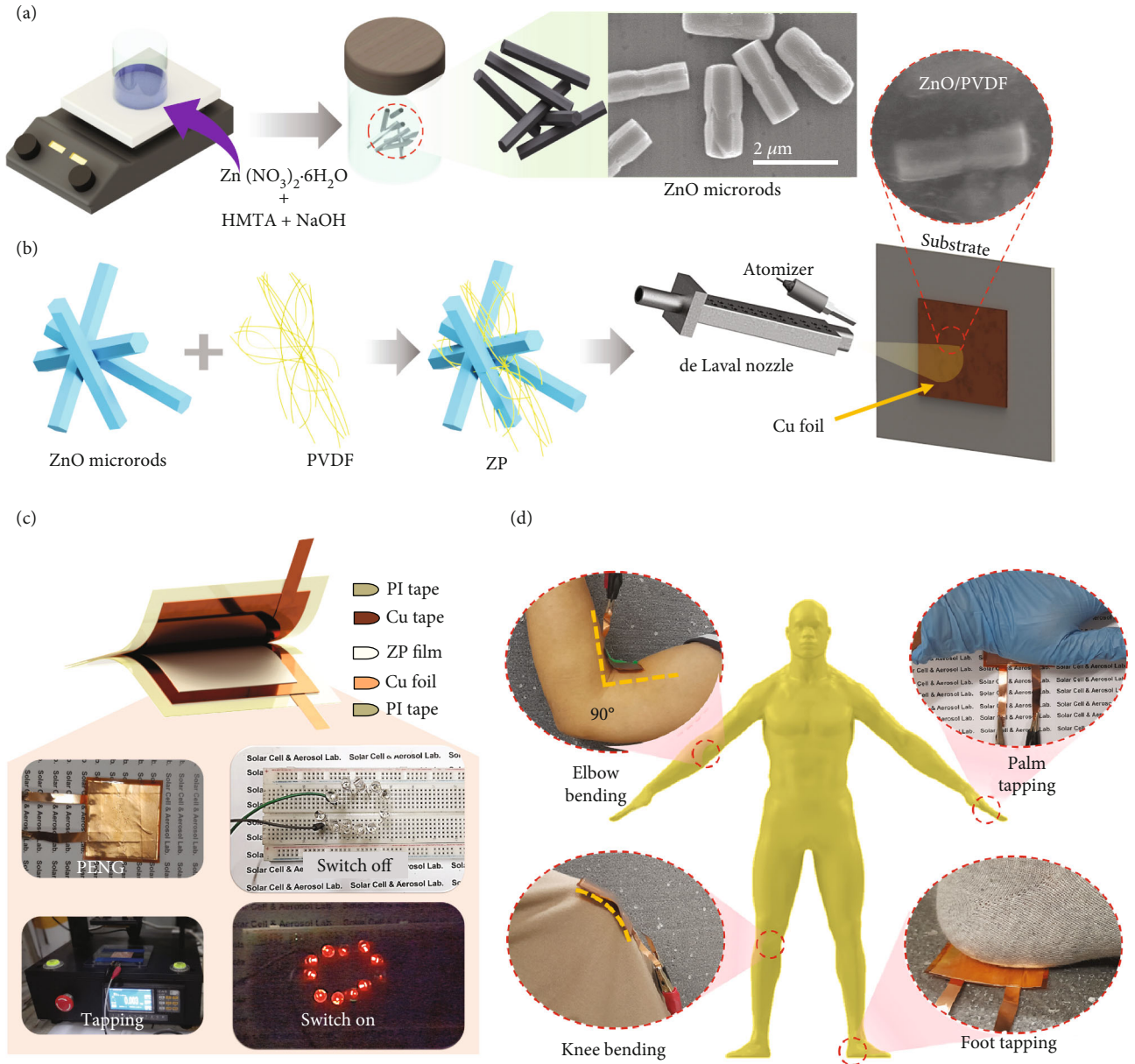


FIGURE 1: Fabrication process and application of the ZP-based PENG: (a) synthesis process of ZnO microrods; (b) supersonic spraying of the ZP composite; (c) fabrication and LED test of ZP5-based PENG; (d) energy harvesting using the PENG via body movements.

insulated using a nonconductive polyimide tape (Figure 1(c)). A tapping instrument (Piezoelectric Generator Measurement System, SnM, Republic of Korea), bending machine (Ocean Science, Coad. 722, Republic of Korea), and oscilloscope (DS1052E, RIGOL, China) were used to explore the kinetic energy-harvesting performance of the ZP-based PENGs. To measure the current and power, different load resistances (0.01–10 M Ω) were connected in series to the PENG. As shown in Figure 1(d), the flexible PENG can be used on various parts of the human body, including elbows, palms, knees, and feet.

2.5. Electrochemical Measurements. Next, we investigated the feasibility of using the ZnO microrods as energy storage materials. We mixed 0.5 g of ZnO microrods, 0.3 mL of

TABLE 1: Fabrication of ZP-based composite films using the supersonic spraying method^a.

ZP composite film	ZnO (g)	PVDF (g)	DMF (mL)
ZP4	0.40	1.0	30
ZP5	0.50	1.0	30
ZP6	0.60	1.0	30

^aPreheating temperature: 250°C; flow rate: 1.5 mL/min.

8 wt% PAN/DMF solution, and 0.1 g reduced graphene oxide (rGO) in 30 mL DMF and stirred the mixture for 10 h. The resulting suspension was then deposited on a Ni foil using a supersonic spraying method, as discussed in Section 2.3. The ZnO/rGO composite film-coated Ni foil was

annealed in an Ar environment at 500°C for 1 h at a heating rate of 3°C/min. The annealed specimens were punched into circles with a diameter of 14 mm and used as electrodes in a CR2032 symmetric coin cell. A 6M KOH was used as the electrolyte, and both electrodes were electrically separated using a polymer membrane (Celgard, 3501, Chungbuk) [44]. Electrochemical measurements were conducted using cyclic voltammetry (CV) and galvanostatic charge-discharge (GCD) measurements. A VersaSTAT-3 potentiostat (Princeton Applied Research, USA) with a two-electrode symmetric cell system was used for the CV measurements. GCD measurements were conducted using a battery cycler (WBCS3000, WonATech Inc.).

2.6. Characterizations. The crystallinity of the ZnO microrods and the resulting ZP composite films were investigated using X-ray diffraction (XRD, SmartLab, Rigaku, Japan) considering Cu-K α radiation ($\lambda = 1.5406 \text{ \AA}$) at a rate of 2°/min. Fourier-transform infrared spectroscopy (FTIR; Spectrum GX, PerkinElmer Inc., USA) was used to analyze the interaction between ZnO and PVDF in the ZP-based composite films. The vibrational mode study confirms the structural transformation of PVDF from the α phase to the β phase [45]. Raman spectra were obtained using a Raman spectrometer and 532 nm laser (LabRam ARAMIS IR2, HORIBA Jobin Yvon, Japan) to observe the influence of ZnO microrods on the phases of PVDF. X-ray photoelectron spectroscopy (XPS; Thermo Fisher Scientific Co., USA) was performed with monochromatic Al K α as an X-ray source to analyze the chemical state of the specimens. The morphology of the ZnO was examined using field-emission scanning electron microscopy (FE-SEM; S-5000, Hitachi, Ltd., Japan) and transmission electron microscopy (TEM; JEM 2100F, JEOL, Inc., Japan). The specimens were prepared for TEM analysis using the focused ion beam technique (FEI Helios G4 UX, Thermo Fisher Scientific, USA). The elemental mapping of the specimens was performed using an energy-dispersive spectrometer (EDS) installed in the transmission electron microscope. High-resolution TEM (HRTEM) and selective area electron diffraction (SAED) were performed to confirm the crystal structures of the specimens. Atomic force microscopy (AFM; XE-100, Park System, South Korea) was performed in the piezoelectric force microscopy (PFM) mode to analyze the surface roughness and effective piezoelectric coefficient.

3. Results and Discussion

3.1. Physicochemical Characterizations. The XRD patterns of the pure ZnO microrods and ZP-based composite films were analyzed to explore their crystallinities (Figure 2(a)). The diffraction patterns of the ZnO microrods were observed at the Bragg angles (2θ) of 31.5°, 34.2°, 36.2°, 47.4°, 56.5°, 62.7°, 66.3°, and 67.8°, corresponding to the (100), (002), (101), (102), (110), (103), (200), and (201) lattice planes of hexagonal wurtzite ZnO, respectively (JCPDS 36-1451) [46]. Furthermore, the XRD patterns of the ZP-based composite films revealed typical and distinct ZnO diffraction peaks of PVDF at 18.4°, 20.1°, and 20.9°, corresponding to the semicrys-

talline nature of PVDF. The most prominent peak, observed at 20.1°, represents the (110) plane of PVDF; particularly, this peak corresponds to the β phase of PVDF and is associated with the piezoelectric characteristics of PVDF [47].

The FTIR spectra of the composite films were characterized to compare the interactions of the ZnO microrods and chemical environment of the PVDF phases. The FTIR spectra of pristine PVDF, ZP4, ZP5, and ZP6 are presented in Figure 2(b). The peaks at 613, 761, 796, 975, and 1381 cm^{-1} are assigned to the nonpolar α phase of PVDF, whereas the peaks observed at 839, 1275, and 1457 cm^{-1} are assigned to the β phase [48, 49]. The characteristic vibrational peak of the β phase at 839 cm^{-1} corresponds to CH₂ rocking, CF₂ stretching, and skeletal C-C stretching, whereas that at 1275 cm^{-1} corresponds to CF out-of-plane deformation [49]. The incorporation of ZnO microrods into the PVDF matrix led to the sharpening of peaks related to the β phase of PVDF. Specifically, with an increase in the number of ZnO microrods, the peaks at 839 and 1275 cm^{-1} became more prominent, whereas the peak at 761 cm^{-1} decreased in the cases of the ZP4-, ZP5-, and ZP6-based composite films (Figure 2(b)). The β phase fraction of the composite films was calculated based on the characteristic absorbance peaks of the α and β phases using Eq. (1) [49]

$$F_{(\beta)} = \frac{A_{\beta}}{(K_{\beta}/K_{\alpha})A_{\alpha} + A_{\beta}} \times 100, \quad (1)$$

where $F_{(\beta)}$ denotes the percentage composition of the electroactive β phase, A_{α} and A_{β} denote the area of absorbance peaks at 761 and 839 cm^{-1} , respectively, and 1.26 is the ratio of the absorbance coefficient of the β phase (K_{β}) at 839 cm^{-1} ($7.7 \times 10^4 \text{ cm}^2 \text{ mol}^{-1}$) to that of the α phase (K_{α}) at 761 cm^{-1} ($6.1 \times 10^4 \text{ cm}^2 \text{ mol}^{-1}$). The β phase amounts of the pristine PVDF-, ZP4-, ZP5-, and ZP6-based composite films were 37.1%, 42.2%, 47.0%, and 45.5%, respectively. This result indicates that the β phase concentration of the PVDF polymer increased owing to the effective interaction between the ZnO microrods and PVDF molecules. Various fabrication processes, e.g., electrospinning, solvent casting, and spin coating, contribute to the phase transformation of PVDF polymers owing to polymer chain stretching or elongation in the presence of fillers [50]. Similarly, β phase enhancement is possible owing to the stretching of PVDF in the presence of a filler (ZnO) during supersonic spraying. In contrast to ZP4 and ZP5, ZP6 composite films exhibit a slight reduction in the β phase, which could be attributed to the reduced stretching of PVDF in a dense ZP precursor solution [51].

In addition to the XRD and FTIR analyses, the ZP-based composite films were studied using Raman spectroscopy. The Raman spectra of the ZP4-, ZP5-, and ZP6-based composite films were obtained in the range of 600–1500 cm^{-1} to analyze the influence of the ZnO microrods on the PVDF matrix (Figure 2(c)). With an increase in the number of ZnO microrods, the Raman bands related to the α phase at 796.8 and 876.3 cm^{-1} were diminished, whereas the Raman band at 840 cm^{-1} corresponding to the β phase was enhanced. This observation shown in the inset of

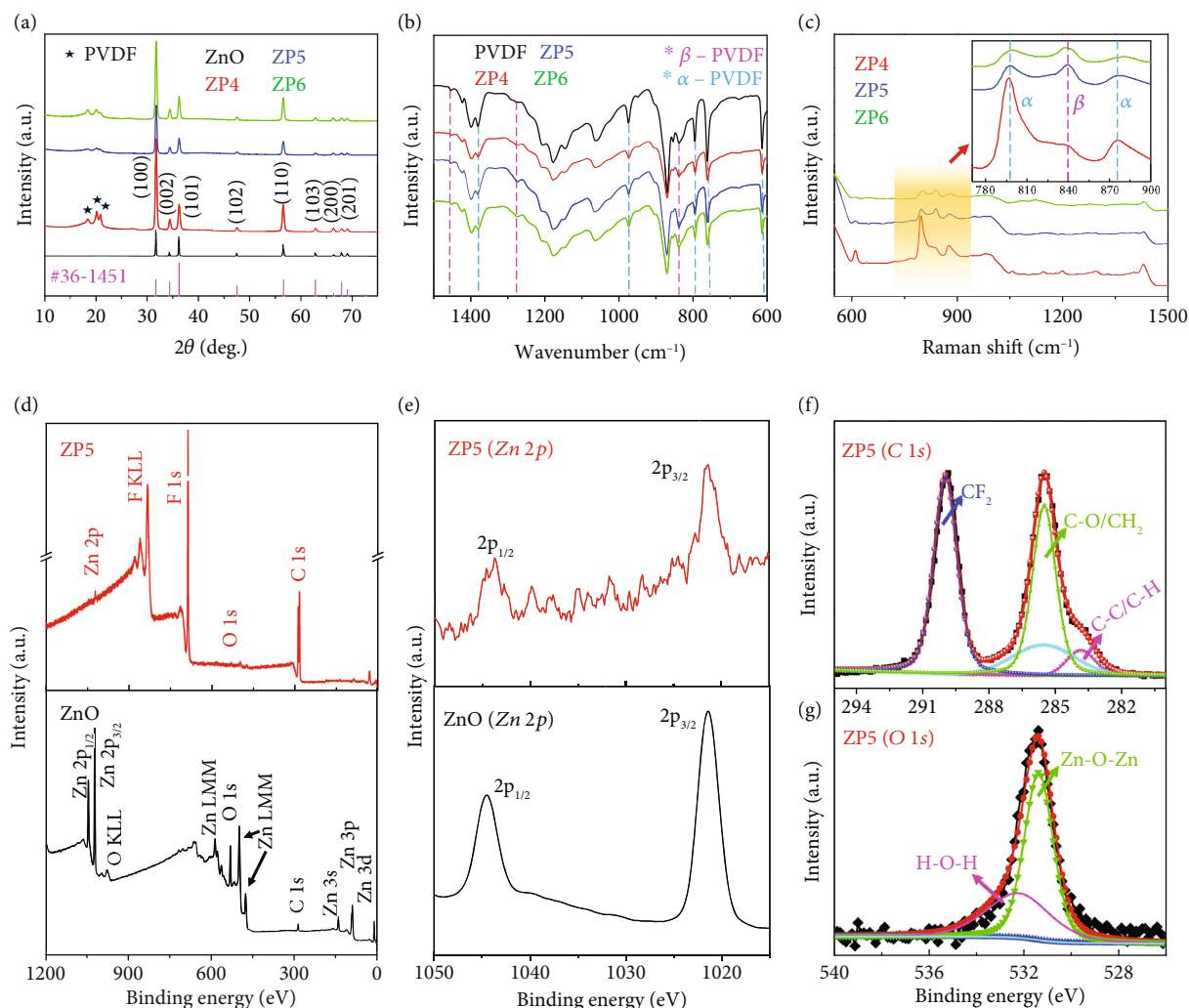


FIGURE 2: (a) XRD patterns of ZnO microrod powder, ZP4, ZP5, and ZP6 films. (b) FTIR spectra of PVDF, ZP4, ZP5, and ZP6 films. (c) Raman spectra of ZP4, ZP5, and ZP6 films (inset showing the enlarged portion in 770–900 cm^{-1}). (d) XPS survey spectra of the ZnO microrods and ZP5 film (red). (e) Zn 2p core-level spectra of the ZnO microrod powder and ZP5 film. (f) C 1s core-level spectra of the ZP5 film. (g) O 1s core-level spectra of the ZP5 film.

Figure 2(c) illustrates the enlarged spectra in the range of 770–900 cm^{-1} . The peak at 1430 cm^{-1} corresponds to the three phases of the PVDF polymer. As the α -peak intensities diminished with an increase in the ZnO content and the β phase intensities increased, the all-transplanar zigzag (TTTT) conformation increased [30, 52].

According to the FTIR results, ZP5 with 0.5 g of ZnO microrods exhibited the highest percentage of β phase PVDF, and hence, its elemental oxidation states were analyzed using XPS. The surface chemical composition and interfacial interaction between ZnO and PVDF were investigated in the binding energy range of 0–1200 eV. The XPS survey spectra (Figure 2(d)) of the synthesized particles and ZP5 confirm the presence of Zn and O. Moreover, the XPS survey spectrum of ZP5 indicates the dominant presence of C and F originating from PVDF. XPSPEAK41 was used to analyze the core XPS spectra of various elements by subtracting the Shirley background. The Zn 2p core spectrum of the ZnO powder exhibits spin-orbital splitting in Zn

$2p_{3/2}$ and Zn $2p_{1/2}$, with peaks at 1021.4 and 1044.5 eV, respectively (Figure 2(e)) [53, 54]. Furthermore, the binding energy difference between the two orbital levels is 23.1 eV, confirming the existence of the Zn²⁺ oxidation state of ZnO [54]. The core spectrum of the ZP5 film for Zn exhibits a slight shift in the binding energies of Zn $2p_{3/2}$ (1021.2 eV) and Zn $2p_{1/2}$ (1044.2 eV). This indicates that the Zn²⁺ atoms originating from ZnO are inclined toward PVDF owing to their affinity for CF_2 . The C 1s core spectrum of ZP5 exhibits two dominant peaks at 290 and 285.5 eV, corresponding to $-\text{CF}_2-$ and $-\text{CH}_2-$ (Figure 2(f)). The deconvoluted peaks at 283.9, 285.4, and 286.7 eV correspond to C–C, CH_2 , and C–O, respectively [55]. Figure 2(g) shows two peaks in the deconvoluted O 1s core level spectrum of the ZP5-based composite film. The peak at 531.4 eV corresponded to covalently bonded Zn–O–Zn, indicating the presence of ZnO microrods in the PVDF matrix [56]. Another peak at 532.2 eV was attributed to the externally adsorbed H–O–H [3, 57]. The XPS spectra of F 1s (Figure S1) for the ZP5-

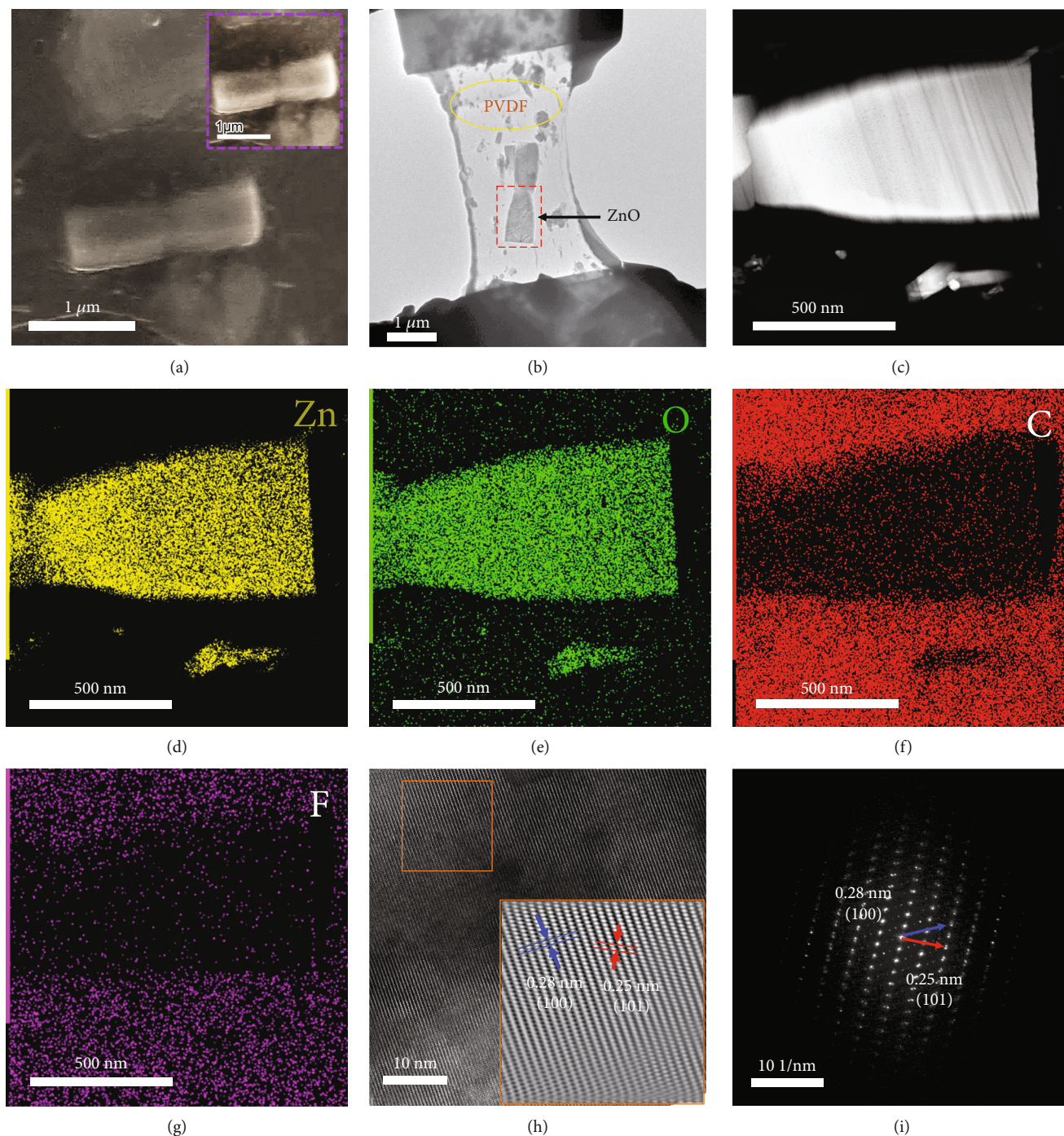


FIGURE 3: (a) SEM image of the ZP5 composite film, including the SEM image of a single ZnO microrod in the inset. (b) TEM image of the ZP5 composite film, exhibiting the enlarged portion of the ZP5 composite film. (c) High-angle annular dark-field image. (d–g) Elemental mapping of the ZP5 composite film, exhibiting Zn, O, C, and F. (h) HRTEM image with lattice fringes, exhibiting the (101) and (100) planes of ZnO microrods. (i) SAED pattern of ZnO microrods with lattice planes.

based composite exhibit a peak corresponding to $-\text{CF}_2-$, located at 687.5 eV, and possessed a lower binding energy than that of the pure PVDF polymer. The shift indicates that the β phase orientation of the PVDF polymer improves owing to ZnO-PVDF interactions [58].

The SEM images of the ZnO microrods and ZP5-based composite films are shown in Figure 3(a). The length and width of the ZnO microrods synthesized using the wet

chemical method at 80°C were $2\ \mu\text{m}$ and approximately 500 nm, respectively. Figure 3(b) shows the TEM images of the highly crystalline ZnO microrods embedded in the PVDF matrix. The high-angle annular dark-field imaging output used for elemental analysis is shown in Figure 3(c). The elemental analysis of the ZP5-based composite film exhibited the presence of Zn, O, C, and F, as indicated by their respective color maps in Figures 3(d)–3(g), respectively,

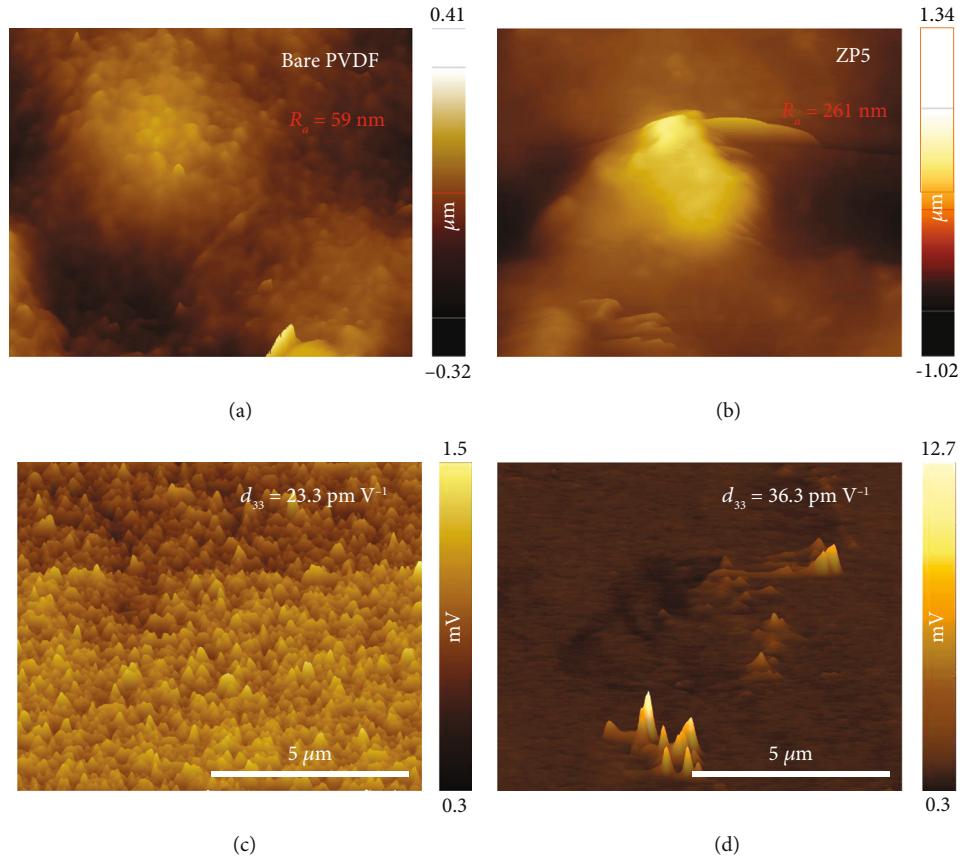


FIGURE 4: PFM images showing the topography of (a) bare PVDF and (b) ZP5. Amplitude measurements of (c) bare PVDF and (d) ZP5 composite film with a scanning area of $10 \mu\text{m} \times 10 \mu\text{m}$.

thereby confirming the presence of the ZnO microrods and PVDF in the ZP5-based composite film. In addition, the HRTEM image and SAED patterns were investigated to analyze the crystal phase and orientation of the ZnO microrods. Diffraction patterns with well-defined lattice fringes were observed based on the HRTEM image (Figure 3(h)). The distances between two lattice fringes, known as interplanar d -spacings, were 0.25 and 0.28 nm, as marked in the enlarged HRTEM images of Figure 3(h); these values correspond to the (101) and (100) lattice fringes of hexagonal wurtzite ZnO, respectively [59]. The interplanar d -spacing was calculated as the reciprocal of the distance between the central bright spot and the other diffraction spots in the SAED pattern (Figure 3(i)). Thus, the calculated d -spacing values of 0.25 and 0.28 nm were assigned to the (101) and (100) lattice planes, respectively [59]. These results agree well with the XRD patterns shown in Figure 2(a).

The piezoelectric properties of ZP5, which possessed the highest β phase content, and a PVDF film were determined using PFM to evaluate the improvement in the piezoelectric characteristics of the composite film owing to the presence of ZnO. PFM can effectively probe local polarization and determine piezoelectric coefficients [60]. The PFM measurements of the PVDF- and ZP5-based composite films were conducted using a Pt-Cr-coated cantilever (Multi75E_G) as an AFM tip. A change in the electric potential between

the sample and AFM tip occurred during the electromechanical response owing to the converse piezoelectric effect (Figure 4). A $10 \mu\text{m} \times 10 \mu\text{m}$ area of the ZP5-based composite film was scanned at an external bias voltage of 10 V and 1 Hz. Figure 4 shows the surface topography and PFM out-of-plane amplitude for the pristine PVDF- and ZP5-based composite films. The pristine PVDF film (Figure 4(a)) exhibits a smooth surface with a roughness value (R_a) of 59 nm. The topographical image of ZP5 (Figure 4(b)) exhibits a considerable increase in roughness (261 nm) owing to the incorporation of ZnO microrods into the PVDF matrix. The amplitude image (Figure 4(c)) of the PVDF sample exhibits nearly uniform bright regions, considering an average amplitude of 0.872 mV. The mean amplitude of the ZP5 film (Figure 4(d)) is 1.356 mV, which is higher than that of the pristine PVDF film. This indicates that the piezoelectric surface potential increased for the ZP5 composite film with ZnO microrods. The piezoelectric coefficient (d_{33}) values of the bare PVDF and ZP5-based composite films can be measured based on the strain produced at an applied voltage. The piezoelectric coefficient (d_{33}) (pm V^{-1}) was obtained based on the PFM analysis using Eq. (2) [60, 61]

$$d_{33} = \frac{D}{V_{AC}}, \quad (2)$$

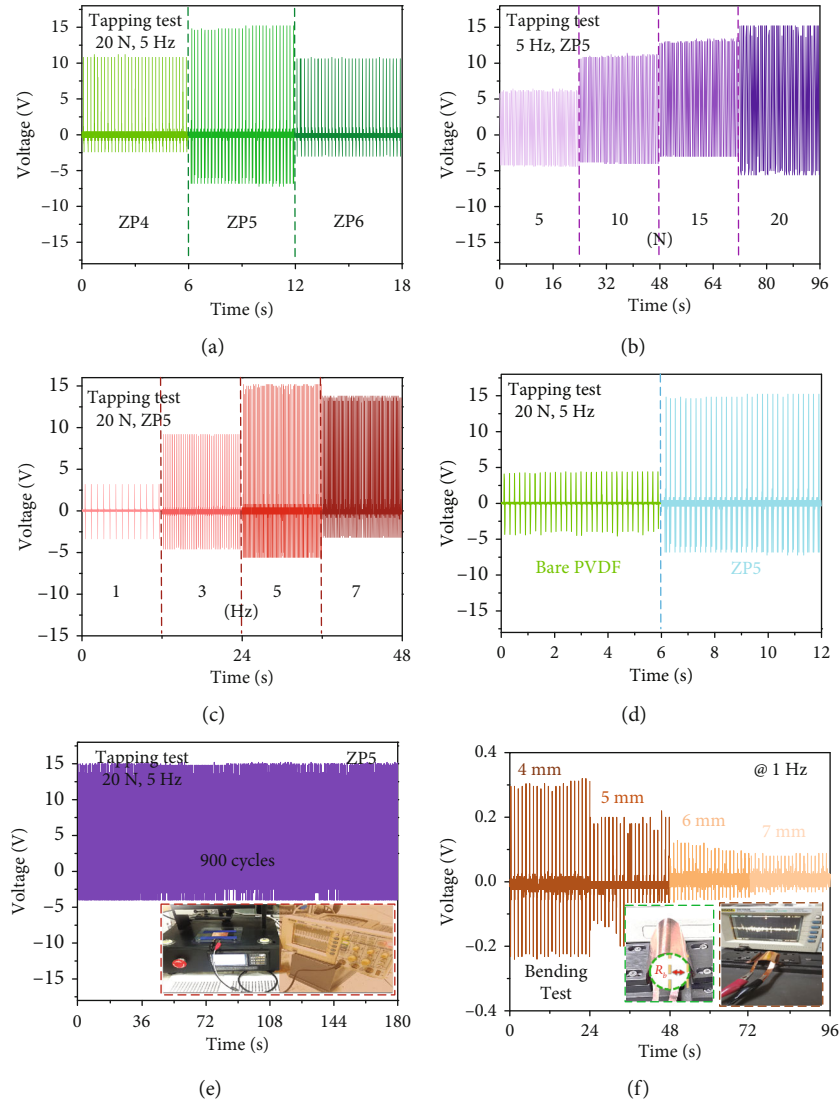


FIGURE 5: Voltage signals of ZP-based PENGs under tapping tests: (a) V vs. t for ZP-based PENGs with varying ZnO microrod content: ZP4, ZP5, and ZP6 composite films; (b) V vs. t with different tapping forces; (c) V vs. t with different tapping frequencies; (d) V of ZP5-based PENG compared with that of bare PVDF-based PENG; (e) long-term tapping test of ZP5-based PENG up to 900 cycles; (f) bending test based on the variation in the bending radius of the ZP5-based PENG at 1 Hz.

where D denotes the deflection of the cantilever tip (in meters) between points A and B; D is calculated using the PFM amplitude value. V_{AC} denotes the AC tip bias voltage at 1 V. The calculation of the deflection D is expressed in Eq. S1 of Section S1. The d_{33} values of the bare PVDF and ZP5-based composite films calculated based on the forward-amplitude images were 23.3 and 36.3 pm V^{-1} , respectively. The higher piezoelectric coefficient of the composite indicated higher polarization and enhanced piezoelectric potential [62].

3.2. Piezoelectric Performance of ZnO/PVDF-Based Composite Materials. Figure 5(a) shows the open-circuit potential (V_{oc}) values of the ZP4-, ZP5-, and ZP6-based PENGs under a tapping force of 20 N at 5 Hz. The V_{oc} values of the ZP4-, ZP5-, and ZP6-based PENGs were 11.2, 15.2, and 10.8 V, respectively. The higher V_{oc} value of ZP5 indi-

cates that the 0.5 g of ZnO included in the precursor was optimal. The force distribution impact varied with the content of ZnO microrods and electroactive β phase in PVDF, which is confirmed by the increase in the piezopotential of ZP5. In the case of ZP6-based PENG, the piezopotential reduced under the same force (20 N) owing to the decrease in the β phase in the PVDF matrix, as confirmed by the FTIR analysis. Consequently, the piezoelectric performance of ZP5 was investigated in detail. The V_{oc} values of the ZP5-based PENG at a tapping force frequency of 5 Hz under varying force magnitudes of 5, 10, 15, and 20 N were 6.1, 11.0, 13.1, and 15.2 V, respectively (Figure 5(b)). This observation indicates that as the mechanical force increases, the piezoelectric potential increases. The increase in V_{oc} was closely related to the increase in the number of dipoles caused by the higher mechanical strain imparted on ZnO and PVDF in the compressed state. A higher compression

TABLE 2: ZnO- and PVDF-based composite films used for PENG fabrication.

Year	Synthesis method	Polymer matrix	Size length (diameter) (nm)	Force (N)	Frequency (Hz)	Voltage (V)	Power ($\mu\text{W cm}^{-2}$)	Ref.
2006	Vapor-liquid-solid (VLS)		200-500		10 MHz	0.008	10 pW μm^{-2}	[20]
2019	Hydrothermal+electrospinning					3.2		[31]
2019	Hydrothermal+electrospinning	PVDF	1500 (120)	21	7	0.356	0.12	[66]
2021	Hydrothermal+electrospinning	PAN	3000 (140)	10		1.60	5.86	[22]
2021	Hydrothermal+electrospraying	PVDF	228 (31)	0.10 MPa	1	14.30		[67]
2021	Hydrothermal+aerosol spray coating	PEDOS:PPS	2000 (150)		26	1.32	0.67	[68]
2023	Wet chemical+supersonic spraying	PVDF	2000 (300)	20	7	15.2	12.5	Present

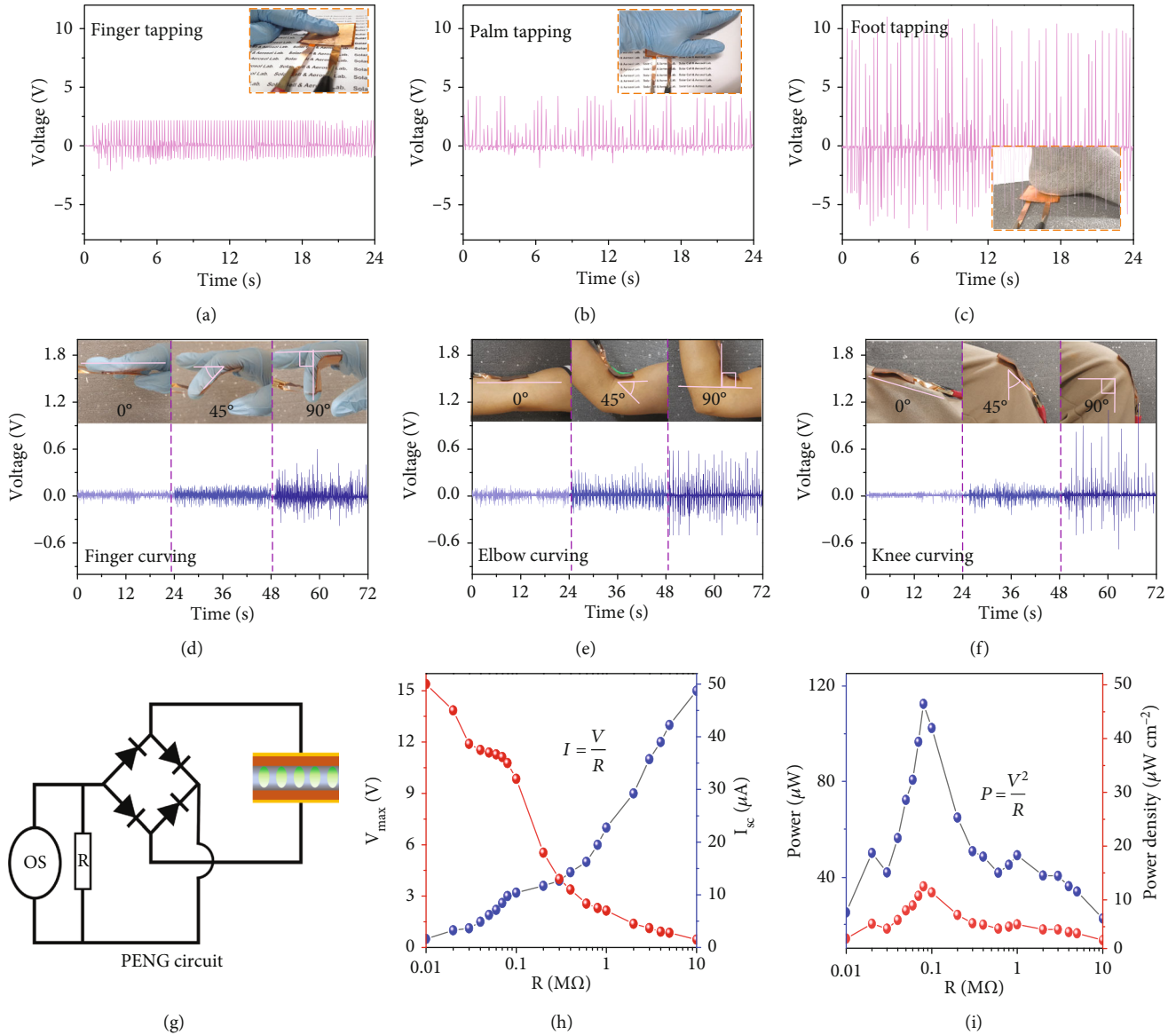


FIGURE 6: Voltage signals of the ZP5-based PENG for different body movements: (a) finger tapping, (b) palm tapping, and (c) foot tapping. Bending at different angles when attached with (d) finger, (e) elbow, and (f) knee. (g) ZP5-based PENG electric circuit for measuring V at different load resistances, (h) measurement of V_{\max} and I_{\max} at various external load resistances, and (i) calculation of power and power density at various external load resistances.

leads to a higher amount of polarized charge at the interfacial sites of ZnO and PVDF [63].

Similarly, the tapping frequency-dependent piezoelectric potential was evaluated under a constant tapping force of 20 N (Figure 5(c)). At 1, 3, 5, and 7 Hz, the output voltage increased owing to the rapid tapping of the ZP5-based PENG. The V_{oc} value at 1 Hz was 3.2 V and gradually increased to 15.2 V at 5 Hz, subsequently decreasing to 13.8 V at 7 Hz. The maximum V_{oc} values were obtained at 20 N and 5 Hz. This observation can be attributed to fast polarization and the remnant electrons in the composite film. However, rapid tapping may result in insufficient time for restoring the polarized dipoles to their original forms, thereby decreasing the voltage at 7 Hz [64, 65]. Accordingly, a bare PVDF film-based PENG was tested to confirm the enhanced piezoelectric

behavior originating from the ZnO microrods. The V_{oc} value of the bare PVDF film-based PENG was 4.3 V, which is approximately one-third of that of ZP5-based PENG (Figure 5(d)). The V_{oc} value of ZP5-based PENG measured over 900 tapping cycles (Figure 5(e)) exhibited a stable, consistent value of ~ 15 V, indicating that the device possesses good piezoelectric stability. The inset of Figure 5(e) shows the tapping machine and oscilloscope. Table 2 lists the comparative results of previous PENGs and the current supersonic sprayed PENG, thereby demonstrating the superior performance of the current PENG.

The piezoelectric behavior was evaluated based on bending tests at different bending radii. Figure 5(f) shows the bending test performed for the ZP5-based PENG with bending radii (R_b) of 4, 5, 6, and 7 mm at 1 Hz; the output

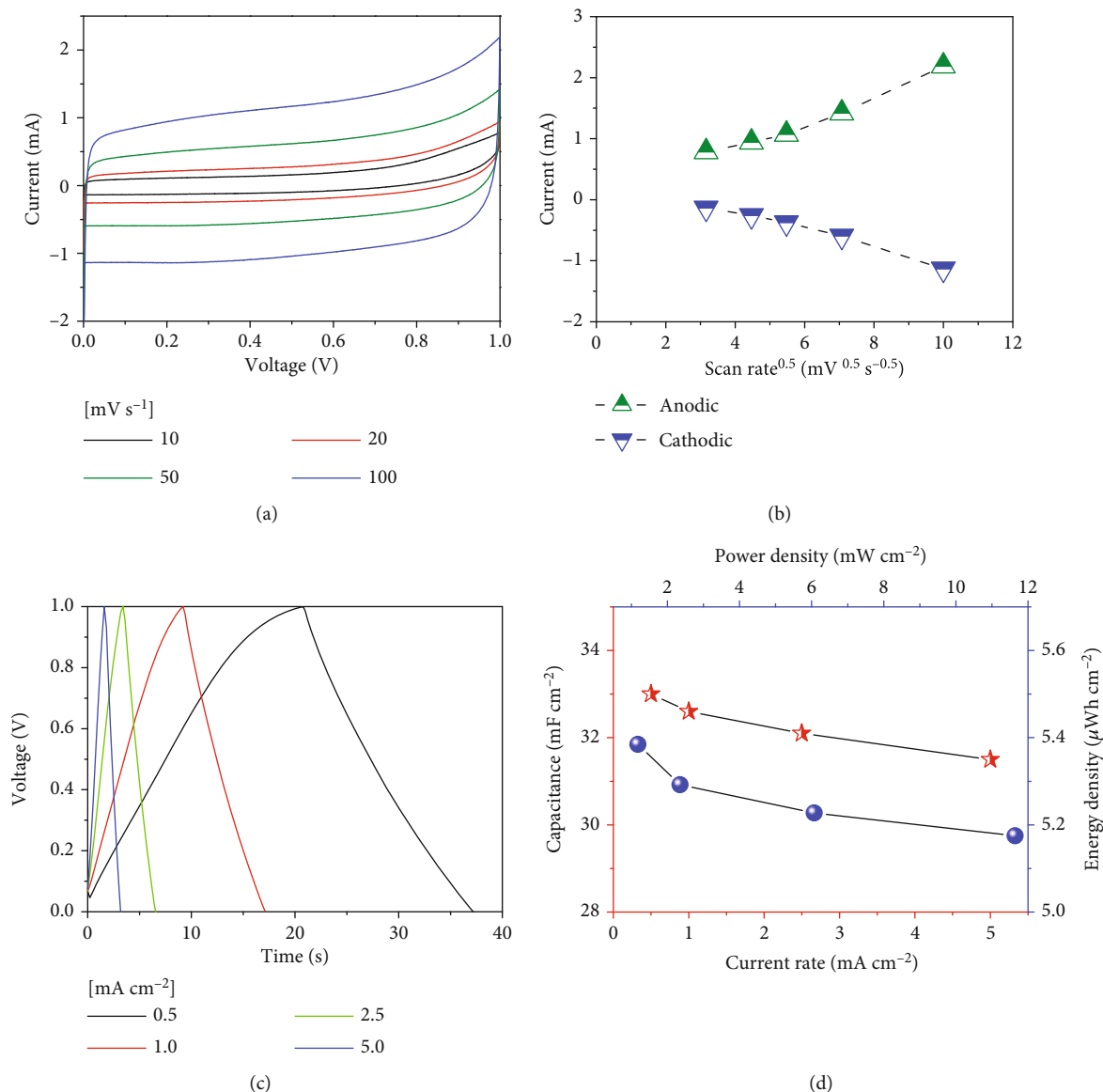


FIGURE 7: Electrochemical measurement of a symmetric coin cell prepared from ZnO microrods embedded with rGO nanosheets: (a) CV plots of the electrode for various scan rates; (b) anodic and cathodic peak current vs. square root of the scan rates in the potential window of 0 to 1.0 V; (c) GCD plots of ZnO microrods covered with rGO sheets at various current densities; (d) specific capacitance, energy density, and power density of the electrode.

voltages were 320, 219, 128, and 90 mV, respectively. As the slider in the bending machine moved inward, the bending radius of the flexible ZP5-based PENG decreased, thereby generating piezoelectric potential owing to the relative displacement of atoms within the composite film; this led to a higher voltage because of the internal strain of the composite film. In the flat position, no piezoelectric voltage was generated. The piezoelectric voltage produced during bending was caused by elastic deformation due to the internal strain of the piezoelectric ZnO microrods [69]. The internal strain during bending was not comparable to the strain produced during tapping. This resulted in a lower V_{oc} [70].

To explore the energy-harvesting and voltage generation performance of the ZP5-based PENG during kinetic motions, we considered mechanical motions and body

vibrations for potential motion-powered energy-harvesting applications (Figures 6(a)–6(f)). The maximum V_{oc} values recorded for finger tapping (Figure 6(a)), palm tapping (Figure 6(b)), and foot tapping (Figure 6(c)) were 2.20, 4.40, and 11.0 V, respectively. These values agree with the previous tapping results, indicating that V_{oc} is directly proportional to the applied mechanical force [71]. In addition, body stretching tests, e.g., finger, elbow, and knee bending, were performed at various bending angles. Specifically, the bending tests were performed at 0° , 45° , and 90° (Figures 6(d)–6(f)). At 0° , no V_{oc} was observed, whereas continuous periodic finger bending at 45° and 90° resulted in maximum V_{oc} values of 165 and 500 mV, respectively. Similarly, elbow bending at 45° and 90° produced 420 and 580 mV, respectively, whereas for knee bending at the same

angles, the V_{oc} values were 250 mV and 1 V, respectively. These results indicate that ZP5-based PENG can harvest small-scale mechanical energy from human body movements, thus demonstrating its potential for practical applications.

The output current (I) was calculated based on the measured maximum piezopotential across the load resistance for the ZP5-based PENG (Figure 6(g)). The maximum output voltage (V_{max}) was recorded by varying the external load resistance R in the electrical circuit (Figure 6(h)). A periodic tapping test was performed under a tapping force of 20 N at 5 Hz to measure the electric signals. The graph in Figure 6(h) illustrates the V_{max} and I_{max} values obtained with external resistances in the range of 0.01–100 M Ω . Figure 6(i) shows that a maximum power of 112.5 μ W was obtained at 0.08 M Ω , and the power density of the ZP5-based PENG with an area of 3 cm \times 3 cm was 12.5 μ W cm $^{-2}$ [72]. Moreover, the performance of the ZP5-based PENG was further investigated by lighting commercial LEDs based on the continuous tapping of the device at 20 N and 5 Hz (Figure 1(c)). These findings reveal the possibility of using the developed ZP-based PENG as a touch sensor and in LED lighting. The long-term cycling test under tapping and bending suggests the excellent durability of the PENG. The energy generated by the physical body activities was harnessed by attaching the PENG to the finger, forearm, and knee, confirming the flexibility of the ZP film, which yielded sufficient output voltage to power microelectronic devices.

The electrochemical properties of ZnO/rGO (Section 2.5) were explored by CV and GCD using a two-electrode symmetric coin cell. The CV measurements were performed at scan rates of 10, 20, 50, and 100 mV s $^{-1}$ with a potential window of 0–1.0 V for the symmetric supercapacitor. Figure 7(a) displays the current as a function of the applied voltage at different scan rates, where near-rectangular CV curves are observed. These quasirectangular curves indicated the pseudocapacitive characteristics of the ZnO microrods coupled with rGO sheets. Figure 7(b) shows the anodic and cathodic curves as square root functions of the scan rate. The positive and negative curves denote anodic and cathodic peak currents, respectively. The linearity of the peak current in the graph indicated the occurrence of reversible faradaic reactions [16]. The GCD technique was used to calculate specific capacitance associated with ZnO covered with rGO. The potential response was recorded at a constant current density (Figure 7(c)). The applied constant current density ranged from 0.5 to 5 mA cm $^{-2}$. The GCD results revealed a discharge time of 16.4 s at 0.5 mA cm $^{-2}$. The plots of the charge and discharge cycles with variations in current density exhibited a nearly triangular shape, indicating that the electrode possesses good capacitive properties. Figure 7(d) shows the capacitance, energy density, and power density with respect to the specific current obtained from the GCD measurements. The maximum areal-specific capacitance was 33 mF cm $^{-2}$. Furthermore, the corresponding maximum energy and power densities were 5.38 μ Wh cm $^{-2}$ and 1.16 mW cm $^{-2}$, respectively. The calculations of capacitance, energy density, and power density are expressed in Eqs. (S2),

(S3), and (S4), respectively (Section S2). The relatively poor electrochemical performance of ZnO/rGO implies that further optimization of the fabricated electrode is necessary.

4. Conclusion

In this study, a flexible, durable, self-powered PENG electrode was fabricated using a supersonic spraying deposition technique. Inorganic piezoelectric ZnO microrods and PVDF polymer were combined to enhance their piezoelectricity and power density. The concentrations of the ZnO microrods and PVDF polymer were optimized to obtain the ZP composite, thereby exhibiting the maximum open circuit potential of 15.2 V and power density of 12.5 μ W cm $^{-2}$. The flexibility and mechanical durability of the PENG were demonstrated via bending and tapping tests.

Data Availability

The numerical data used to support the findings of this study are available from the corresponding authors on reasonable request.

Conflicts of Interest

The authors declare that they have no conflicts of interest.

Authors' Contributions

Devi Prashad Ojha, Bhavana Joshi, and Edmund Samuel contributed equally to this work.

Acknowledgments

This work was supported by the National Research Foundation of Korea (NRF) grant funded by the Korea government (MSIT) (NRF-2020R1A5A1018153, NRF-2021R1A2C2010530, and 2022M3J1A106422611). The authors acknowledge the King Saud University, Riyadh, Saudi Arabia, for funding this work through Researchers Supporting Project Number RSP2023R30.

Supplementary Materials

The supplementary information file outlines the method for calculating PFM tip deflection (D) for piezoelectric coefficient (d_{33}) measurement; see Eq. S1. Areal capacitance (C), energy density (E), and power density (P) were estimated using Eqs. S2, S3, and S4, respectively. XPS core-level spectra of F 1s of the ZP5 composite film are provided in Figure S1. (*Supplementary Materials*)

References

- [1] H. Kim, K. R. Pyun, M.-T. Lee, H. B. Lee, and S. H. Ko, "Recent advances in sustainable wearable energy devices with nanoscale materials and macroscale structures," *Advanced Functional Materials*, vol. 32, no. 16, article 2110535, 2022.
- [2] S. Kartik, D. Prakash, R. R. Kumar et al., "Betel leaf-derived carbon nano-sphere/renewable resourced polyurethane coatings for high-performance applications," *Polymer Bulletin*, vol. 78, no. 7, pp. 3527–3541, 2021.

- [3] R. Tholkappiyan and K. Vishista, "Structural, optical and magnetic properties of nanocrystalline zinc ferrite particles from glycine assisted combustion: effect of Sr^{2+} dopant," *International Journal of Materials Research*, vol. 106, no. 2, pp. 127–136, 2021.
- [4] Z. L. Wang, "Trielectronic nanogenerator (TENG)—sparking an energy and sensor revolution," *Advanced Energy Materials*, vol. 10, no. 17, article 2000137, 2020.
- [5] Z. Li, G. Zhu, R. Yang, A. C. Wang, and Z. L. Wang, "Muscle-driven in vivo nanogenerator," *Advanced Materials*, vol. 22, no. 23, pp. 2534–2537, 2010.
- [6] A. T. Le, M. Ahmadipour, and S.-Y. Pung, "A review on ZnO-based piezoelectric nanogenerators: synthesis, characterization techniques, performance enhancement and applications," *Journal of Alloys and Compounds*, vol. 844, article 156172, 2020.
- [7] W. Wu, S. Bai, M. Yuan, Y. Qin, Z. L. Wang, and T. Jing, "Lead zirconate titanate nanowire textile nanogenerator for wearable energy-harvesting and self-powered devices," *ACS Nano*, vol. 6, no. 7, pp. 6231–6235, 2012.
- [8] Y. B. Lee, J. K. Han, S. Noothongkaew et al., "Toward arbitrary-direction energy harvesting through flexible piezoelectric nanogenerators using perovskite PbTiO_3 nanotube arrays," *Advanced Materials*, vol. 29, no. 6, article 1604500, 2017.
- [9] P. Zhang, W. Zhang, L. Deng, and H. Zhang, "A triboelectric nanogenerator based on temperature-stable high dielectric BaTiO_3 -based ceramic powder for energy harvesting," *Nano Energy*, vol. 87, article 106176, 2021.
- [10] G. Zhu, R. Yang, S. Wang, and Z. L. Wang, "Flexible high-output nanogenerator based on lateral ZnO nanowire array," *Nano Letters*, vol. 10, no. 8, pp. 3151–3155, 2010.
- [11] C.-T. Huang, J. Song, W.-F. Lee et al., "GaN nanowire arrays for high-output nanogenerators," *Journal of the American Chemical Society*, vol. 132, no. 13, pp. 4766–4771, 2010.
- [12] A. C. Wang, C. Wu, D. Pisignano, Z. L. Wang, and L. Persano, "Polymer nanogenerators: opportunities and challenges for large-scale applications," *Journal of Applied Polymer Science*, vol. 135, no. 24, article 45674, 2018.
- [13] H. Feng, C. Zhao, P. Tan, R. Liu, X. Chen, and Z. Li, "Nanogenerator for biomedical applications," *Advanced Healthcare Materials*, vol. 7, no. 10, article 1701298, 2018.
- [14] Y. L. Wu, A. I. Y. Tok, F. Y. C. Boey, X. T. Zeng, and X. H. Zhang, "Surface modification of ZnO nanocrystals," *Applied Surface Science*, vol. 253, no. 12, pp. 5473–5479, 2007.
- [15] Q. Zhang, C. S. Dandeneau, X. Zhou, and G. Cao, "ZnO nanostructures for dye-sensitized solar cells," *Advanced Materials*, vol. 21, no. 41, pp. 4087–4108, 2009.
- [16] E. Samuel, B. Joshi, Y.-i. Kim, A. Aldalbahi, M. Rahaman, and S. S. Yoon, "ZnO/ MnO_x nanoflowers for high-performance supercapacitor electrodes," *ACS Sustainable Chemistry & Engineering*, vol. 8, no. 9, pp. 3697–3708, 2020.
- [17] M. Y. Soomro, I. Hussain, N. Bano, O. Nur, and M. Willander, "Piezoelectric power generation from zinc oxide nanowires grown on paper substrate," *Physica Status Solidi (RRL) - Rapid Research Letters*, vol. 6, no. 2, pp. 80–82, 2012.
- [18] T. Ramachandran, S. Natarajan, and F. Hamed, "The role of dysprosium levels in the formation of mixed oxidation states within spinel $\text{MnCo}_{2-x}\text{Dy}_x\text{O}_4$ nanocrystalline powders," *Journal of Electron Spectroscopy and Related Phenomena*, vol. 242, article 146952, 2020.
- [19] R. Tholkappiyan, G. Anandkumar, L. M. Azarudeen, and K. Vishista, "Structural, morphology and luminescence studies on Mn-doped ZnO phosphor," *Advanced Science, Engineering and Medicine*, vol. 6, no. 11, pp. 1205–1209, 2014.
- [20] Z. L. Wang and J. Song, "Piezoelectric nanogenerators based on zinc oxide nanowire arrays," *Science*, vol. 312, no. 5771, pp. 242–246, 2006.
- [21] A. Rasheed, W. He, Y. Qian, H. Park, and D. J. Kang, "Flexible supercapacitor-type rectifier-free self-charging power unit based on a multifunctional polyvinylidene fluoride–ZnO–RGO piezoelectric matrix," *ACS Applied Materials & Interfaces*, vol. 12, no. 18, pp. 20891–20900, 2020.
- [22] Y. Sun, Y. Zheng, R. Wang, J. Fan, and Y. Liu, "Direct-current piezoelectric nanogenerator based on two-layer zinc oxide nanorod arrays with equal c-axis orientation for energy harvesting," *Chemical Engineering Journal*, vol. 426, article 131262, 2021.
- [23] R. Mao, B. Yu, J. Cui et al., "Piezoelectric stimulation from electrospun composite nanofibers for rapid peripheral nerve regeneration," *Nano Energy*, vol. 98, article 107322, 2022.
- [24] S. Bairagi, M. Shahadat, D. M. Mulvihill, and W. Ali, "Mechanical energy harvesting and self-powered electronic applications of textile-based piezoelectric nanogenerators: a systematic review," *Nano Energy*, vol. 111, article 108414, 2023.
- [25] B. Ameduri, "From vinylidene fluoride (VDF) to the applications of VDF-containing polymers and copolymers: recent developments and future trends," *Chemical Reviews*, vol. 109, no. 12, pp. 6632–6686, 2009.
- [26] L. Lu, W. Ding, J. Liu, and B. Yang, "Flexible PVDF based piezoelectric nanogenerators," *Nano Energy*, vol. 78, article 105251, 2020.
- [27] Y. U. N. Ye, Y. Jiang, Z. Wu, and H. Zeng, "Phase transitions of poly(vinylidene fluoride) under electric fields," *Integrated Ferroelectrics*, vol. 80, no. 1, pp. 245–251, 2006.
- [28] S. An, H. S. Jo, G. Li, E. Samuel, S. S. Yoon, and A. L. Yarin, "Sustainable nanotextured wave energy harvester based on ferroelectric fatigue-free and flexoelectricity-enhanced piezoelectric P(VDF-TrFE) nanofibers with BaSrTiO_3 nanoparticles," *Advanced Functional Materials*, vol. 30, no. 25, article 2001150, 2020.
- [29] Y. P. Lim, J. S. C. Koay, J. Zhao et al., "Modulating ZnO growth structures for maximum power output of hybrid piezo/triboelectric nanogenerator," *Advanced Functional Materials*, vol. 32, no. 46, article 2206750, 2022.
- [30] M. Kim, Y. S. Wu, E. C. Kan, and J. Fan, "Breathable and flexible piezoelectric ZnO@PVDF fibrous nanogenerator for wearable applications," *Polymer*, vol. 10, no. 7, p. 745, 2018.
- [31] Z. Li, X. Zhang, and G. Li, "In situ ZnO nanowire growth to promote the PVDF piezo phase and the ZnO–PVDF hybrid self-rectified nanogenerator as a touch sensor," *Physical Chemistry Chemical Physics*, vol. 16, no. 12, pp. 5475–5479, 2014.
- [32] G. Wang, Y. Deng, Y. Xiang, and L. Guo, "Fabrication of radial ZnO nanowire clusters and radial ZnO/PVDF composites with enhanced dielectric properties," *Advanced Functional Materials*, vol. 18, no. 17, pp. 2584–2592, 2008.
- [33] E. Samuel, B. Joshi, M.-W. Kim, M. T. Swihart, and S. S. Yoon, "Morphology engineering of photoelectrodes for efficient photoelectrochemical water splitting," *Nano Energy*, vol. 72, article 104648, 2020.
- [34] H. S. Jo, S. An, C.-W. Park, D.-Y. Woo, A. L. Yarin, and S. S. Yoon, "Wearable, stretchable, transparent all-in-one soft

- sensor formed from supersonically sprayed silver nanowires,” *ACS Applied Materials & Interfaces*, vol. 11, no. 43, pp. 40232–40242, 2019.
- [35] E. Samuel, T.-G. Kim, C.-W. Park, B. Joshi, M. T. Swihart, and S. S. Yoon, “Supersonically sprayed $Zn_2SnO_4/SnO_2/CNT$ nanocomposites for high-performance supercapacitor electrodes,” *ACS Sustainable Chemistry & Engineering*, vol. 7, no. 16, pp. 14031–14040, 2019.
- [36] S. An, B. Joshi, A. L. Yarin, M. T. Swihart, and S. S. Yoon, “Supersonic cold spraying for energy and environmental applications: one-step scalable coating technology for advanced micro- and nanotextured materials,” *Advanced Materials*, vol. 32, no. 2, article 1905028, 2020.
- [37] C. Park, E. Samuel, B. Joshi et al., “Supersonically sprayed $Fe_2O_3/C/CNT$ composites for highly stable Li-ion battery anodes,” *Chemical Engineering Journal*, vol. 395, article 125018, 2020.
- [38] T. Kim, C. Park, E. P. Samuel et al., “Supersonically sprayed washable, wearable, stretchable, hydrophobic, and antibacterial rGO/AgNW fabric for multifunctional sensors and supercapacitors,” *ACS Applied Materials & Interfaces*, vol. 13, no. 8, pp. 10013–10025, 2021.
- [39] B. Joshi, J. Seol, E. Samuel et al., “Supersonically sprayed PVDF and ZnO flowers with built-in nanocuboids for wearable piezoelectric nanogenerators,” *Nano Energy*, vol. 112, article 108447, 2023.
- [40] M. W. Lee, S. An, S. S. Yoon, and A. L. Yarin, “Advances in self-healing materials based on vascular networks with mechanical self-repair characteristics,” *Advances in Colloid and Interface Science*, vol. 252, pp. 21–37, 2018.
- [41] C. Park, T. Kim, Y.-I. Kim, M. W. Lee, S. An, and S. S. Yoon, “Supersonically sprayed transparent flexible multifunctional composites for self-cleaning, anti-icing, anti-fogging, and anti-bacterial applications,” *Composites Part B: Engineering*, vol. 222, article 109070, 2021.
- [42] S. An, B.-H. Bang, M. W. Lee, and S. S. Yoon, “Review of recent progress in the supersonic cold-spraying technique with solid particles and liquid suspensions,” *Experiments in Fluids*, vol. 62, no. 7, p. 145, 2021.
- [43] G. Nie, X. Zhao, J. Jiang et al., “Flexible supercapacitor of high areal performance with vanadium/cobalt oxides on carbon nanofibers as a binder-free membrane electrode,” *Chemical Engineering Journal*, vol. 402, article 126294, 2020.
- [44] C. Park, T. Kim, E. P. Samuel, Y.-I. Kim, S. An, and S. S. Yoon, “Superhydrophobic antibacterial wearable metallized fabric as supercapacitor, multifunctional sensors, and heater,” *Journal of Power Sources*, vol. 506, article 230142, 2021.
- [45] R. Tholkappiyian, R. Sathesh Kumar, L. Mohamed Azaruddeen, G. Anand Kumar, K. Vishista, and F. Hamed, “Facile synthesis of Cr-doped SrS phosphor: an investigations on structural, vibrational, morphological and photoluminescence properties,” *Materials Focus*, vol. 5, no. 4, pp. 342–346, 2016.
- [46] R. Kaur, M. Suresh, J. López-Vidrier et al., “In situ approach to fabricate heterojunction p–n CuO–ZnO nanostructures for efficient photocatalytic reactions,” *New Journal of Chemistry*, vol. 44, no. 45, pp. 19742–19752, 2020.
- [47] Y. Fu, Y. Cheng, C. Chen, D. Li, and W. Zhang, “Study on preparation process and enhanced piezoelectric performance of pine-needle-like ZnO@PVDF composite nanofibers,” *Polymer Testing*, vol. 108, article 107513, 2022.
- [48] M. Sharma, V. Srinivas, G. Madras, and S. Bose, “Outstanding dielectric constant and piezoelectric coefficient in electrospun nanofiber mats of PVDF containing silver decorated multiwall carbon nanotubes: assessing through piezoresponse force microscopy,” *RSC Advances*, vol. 6, no. 8, pp. 6251–6258, 2016.
- [49] X. Cai, T. Lei, D. Sun, and L. Lin, “A critical analysis of the α , β and γ phases in poly(vinylidene fluoride) using FTIR,” *RSC Advances*, vol. 7, no. 25, pp. 15382–15389, 2017.
- [50] A. Gebrekrstos, T. S. Muzata, and S. S. Ray, “Nanoparticle-enhanced β -phase formation in electroactive PVDF composites: a review of systems for applications in energy harvesting, EMI shielding, and membrane technology,” *ACS Applied Nano Materials*, vol. 5, no. 6, pp. 7632–7651, 2022.
- [51] M. Khalifa, S. Peravali, S. Varsha, and S. Anandhan, “Piezoelectric energy harvesting using flexible self-poled electroactive nanofabrics based on PVDF/ZnO-decorated SWCNT nanocomposites,” *Journal of Metals*, vol. 74, no. 8, pp. 3162–3171, 2022.
- [52] P. Martins, A. C. Lopes, and S. Lanceros-Mendez, “Electroactive phases of poly(vinylidene fluoride): determination, processing and applications,” *Progress in Polymer Science*, vol. 39, no. 4, pp. 683–706, 2014.
- [53] R. Tholkappiyian and K. Vishista, “Influence of lanthanum on the optomagnetic properties of zinc ferrite prepared by combustion method,” *Physica B: Condensed Matter*, vol. 448, pp. 177–183, 2014.
- [54] R. Tholkappiyian and K. Vishista, “Synthesis and characterization of barium zinc ferrite nanoparticles: working electrode for dye sensitized solar cell applications,” *Solar Energy*, vol. 106, pp. 118–128, 2014.
- [55] A. Qin, X. Li, X. Zhao, D. Liu, and C. He, “Engineering a highly hydrophilic PVDF membrane via binding TiO_2 nanoparticles and a PVA layer onto a membrane surface,” *ACS Applied Materials & Interfaces*, vol. 7, no. 16, pp. 8427–8436, 2015.
- [56] J. Bennet, R. Tholkappiyian, K. Vishista, N. V. Jaya, and F. Hamed, “Attestation in self-propagating combustion approach of spinel AFe_2O_4 ($A = Co, Mg$ and Mn) complexes bearing mixed oxidation states: magnetostructural properties,” *Applied Surface Science*, vol. 383, pp. 113–125, 2016.
- [57] R. Tholkappiyian and K. Vishista, “NN-methylene bis acrylamide: a novel fuel for combustion synthesis of zinc ferrite nanoparticles and studied by X-ray photoelectron spectroscopy,” *International Journal of ChemTech Research*, vol. 6, pp. 2834–2842, 2014.
- [58] R. Bhunia, A. Yadav, S. Jha et al., “Probing local environment of Mn-doped nanocrystalline-ZnO/PVDF composite thin films by XPS and EXAFS studies,” *Polymer*, vol. 78, pp. 1–12, 2015.
- [59] J. Choi, D. K. Jin, J. Jeong et al., “Facet-selective morphology-controlled remote epitaxy of ZnO microcrystals via wet chemical synthesis,” *Scientific Reports*, vol. 11, no. 1, article 22697, 2021.
- [60] S. Hong, “Single frequency vertical piezoresponse force microscopy,” *Journal of Applied Physics*, vol. 129, no. 5, article 051101, 2021.
- [61] S. Dutta, P. Buragohain, S. Glinsek et al., “Piezoelectricity in hafnia,” *Nature Communications*, vol. 12, no. 1, p. 7301, 2021.
- [62] V. Khurana, R. R. Kisannagar, S. S. Domala, and D. Gupta, “In situ polarized ultrathin PVDF film-based flexible piezoelectric nanogenerators,” *ACS Applied Electronic Materials*, vol. 2, no. 10, pp. 3409–3417, 2020.

- [63] S. Cao, H. Zou, B. Jiang, M. Li, and Q. Yuan, "Incorporation of ZnO encapsulated MoS₂ to fabricate flexible piezoelectric nanogenerator and sensor," *Nano Energy*, vol. 102, article 107635, 2022.
- [64] N. A. Hoque, P. Thakur, P. Biswas et al., "Biowaste crab shell-extracted chitin nanofiber-based superior piezoelectric nanogenerator," *Journal of Materials Chemistry A*, vol. 6, no. 28, pp. 13848–13858, 2018.
- [65] X.-S. Zhang, M.-D. Han, R.-X. Wang et al., "Frequency-multiplication high-output triboelectric nanogenerator for sustainably powering biomedical microsystems," *Nano Letters*, vol. 13, no. 3, pp. 1168–1172, 2013.
- [66] P. Fakhri, B. Amini, R. Bagherzadeh et al., "Flexible hybrid structure piezoelectric nanogenerator based on ZnO nanorod/PVDF nanofibers with improved output," *RSC Advances*, vol. 9, no. 18, pp. 10117–10123, 2019.
- [67] M. Kim and J. Fan, "Piezoelectric properties of three types of PVDF and ZnO nanofibrous composites," *Advanced Fiber Materials*, vol. 3, no. 3, pp. 160–171, 2021.
- [68] Q. He, X. Li, J. Zhang, H. Zhang, and J. Briscoe, "P-N junction-based ZnO wearable textile nanogenerator for biomechanical energy harvesting," *Nano Energy*, vol. 85, article 105938, 2021.
- [69] J. H. He, C. L. Hsin, J. Liu, L. J. Chen, and Z. L. Wang, "Piezoelectric gated diode of a single ZnO nanowire," *Advanced Materials*, vol. 19, no. 6, pp. 781–784, 2007.
- [70] K. Kim, S. Lee, J.-S. Nam et al., "Highly transparent and mechanically robust energy-harvestable piezocomposite with embedded 1D P(VDF-TrFE) nanofibers and single-walled carbon nanotubes," *Advanced Functional Materials*, vol. 33, no. 14, article 2213374, 2023.
- [71] W. Rahman, S. Garain, A. Sultana, T. Ranjan Middy, and D. Mandal, "Self-powered piezoelectric nanogenerator based on wurtzite ZnO nanoparticles for energy harvesting application," *Materials Today: Proceedings*, vol. 5, 3, Part 3, pp. 9826–9830, 2018.
- [72] L. Ye, L. Chen, J. Yu et al., "High-performance piezoelectric nanogenerator based on electrospun ZnO nanorods/P(VDF-TrFE) composite membranes for energy harvesting application," *Journal of Materials Science: Materials in Electronics*, vol. 32, no. 4, pp. 3966–3978, 2021.